Research Square

Preprints are preliminary reports that have not undergone peer review.
They should not be considered conclusive, used to inform clinical practice,
or referenced by the media as validated information.

Severe shrinkage of Earth's magnetosphere during the May 2024 solar storm

Kazuhiro Yamamoto

yamamoto.kazuhiro.s4@f.mail.nagoya-u.ac.jp

Nagoya University

Yoshizumi Miyoshi

Nagoya University

Naritoshi Kitamura

Nagoya University

Rumi Nakamura

Austrian Academy of Sciences

Atsuki Shinbori

Nagoya University

Ayako Matsuoka

Kyoto University

Mariko Teramoto

Kyushu Institute of Technology

Shoichiro Yokota

Osaka University

Satoshi Kasahara

the University of Tokyo

Kunihiro Keika

the University of Tokyo

Tomoaki Hori

Nagoya University

Kazushi Asamura

Japan Aerospace Exploration Agency

Yoichi Kazama

Academia Sinica Institute of Astronomy and Astrophysics

Shiang-Yu Wang

Academia Sinica Institute of Astronomy and Astrophysics

Sunny Wing-Yee Tam

National Cheng Kung University

Tzu-Fang Chang

National Cheng Kung University

Bo-Jhou Wang

Academia Sinica Institute of Astronomy and Astrophysics

Chae-Woo Jun

Nagoya University

Iku Shinohara

Japan Aerospace Exploration Agency

Article

Keywords: May 2024 super geomagnetic storm, solar storm, magnetopause, solar energetic particles (SEPs), magnetospheric current system, Arase (ERG) satellite

Posted Date: April 23rd, 2026

DOI: https://doi.org/10.21203/rs.3.rs-8649685/v1

License: This work is licensed under a Creative Commons Attribution 4.0 International License. Read Full License

Additional Declarations: No competing interests reported.

Abstract

Earth's main magnetic field forms the magnetosphere, a barrier against solar wind plasmas. A southward magnetic field carried by the solar wind makes the magnetosphere smaller, which is termed "magnetopause erosion." This process leads to equatorward extension of the polar region, where solar wind plasmas directly intrude into the magnetosphere. Although previous studies have suggested that magnetopause reconnection causes magnetopause erosion, the erosion mechanism during super geomagnetic storms remains controversial owing to a lack of *in situ* measurements. Here, we report a magnetopause crossing by the Arase satellite at 4.96 R_E during the May 2024 super geomagnetic storm, which is the innermost magnetopause ever detected by magnetospheric spacecraft. An unexpected decrease in the magnetic field intensity extended from the inner magnetosphere to the magnetopause, indicating that magnetospheric currents reduced Earth's main magnetic field on a global scale. Consequently, the solar wind pushed the weakened magnetosphere further toward the Earth, resulting in the severe shrinkage of the magnetosphere. This shrinkage led to a significant equatorward penetration of solar energetic particles on the dayside, suggesting that the magnetospheric currents can increase the risk of aircraft exposure to solar energetic particles at mid-latitudes.

Introduction

The Earth's dayside magnetosphere directly interacts with the solar wind, a supersonic plasma flow ejected from the Sun. This interaction forms a boundary between the Earth's main magnetic field and the interplanetary magnetic field (IMF) embedded in the solar wind, known as the magnetopause[1]. The location and shape of the magnetopause are primarily controlled by the pressure balance between the magnetic field pressure on the magnetospheric side and the dynamic pressure of the solar wind under a northward IMF[1]. The averaged location of the magnetopause is ~ 10 R_E, where R_E is the Earth's radius (6371.2 km)[2]. However, a southward IMF moves the magnetopause closer to the Earth than a northward IMF does[3], a phenomenon referred to as "magnetopause erosion."

Although numerous space-borne measurements have confirmed magnetopause erosion, the mechanism underlying this phenomenon has been debated for decades. Previous studies initially postulated that a southward IMF leads to an enhanced magnetopause reconnection that removes the magnetic flux from the dayside magnetosphere, and that the solar wind plasma further presses the magnetosphere closer to the Earth owing to the weakened magnetic field pressure[3–7]. Conversely, recent global magnetohydrodynamic (MHD) simulations have demonstrated that magnetospheric current systems, such as the Region-1 field-aligned current[8,9] and the nightside cross-tail current[10], generate a southward magnetic field (downward light blue arrows in Fig. 1) and weaken the Earth's main magnetic field, according to Ampere's law. This results in magnetopause erosion as originally proposed by ref. 11,12 with their analytical models of the current systems. Verifying the erosion mechanism during large geomagnetic storms requires *in-situ* observations of a low-latitude magnetopause at noon inside the geosynchronous orbit (at ~ 6.6 R_E) with simultaneous solar wind measurements. Such a coordinated

observation has not previously been achieved during a super geomagnetic storm (i.e., an event with the disturbance storm time index (Dst) [13] of < − 250 nT[14]), in which space weather effects are significantly enhanced and the location of the magnetopause is essential for the space weather forecasting.

For addressing the debate of the magnetopause erosion mechanism, the Exploration of energization and Radiation in Geospace (ERG) mission[15] of the Japan Aerospace Exploration Agency (JAXA) has successfully conducted *in-situ* observations of an intense magnetopause erosion by the Arase satellite during a super geomagnetic storm in May 2024.

Results

Firstly, we provide an overview of the super geomagnetic storm that occurred in May 2024. A solar active region produced numerous X-class solar flares and launched multiple Earth-directed coronal mass ejections (CMEs)[16] between May 5 and 15, 2024. The CMEs launched on May 8 and 9 struck the Earth and caused the super geomagnetic storm between May 10 and 12[17]. The Dst index reached − 406 nT during this storm, which is the largest disturbance in the past 20 years since the November 2003 storm.

Here, we examine the observational data of the Arase satellite during its magnetopause crossing on May 11, 2024. Until 06:52:50 UT (vertical line on the left side in Fig. 2, where UT is Universal Time), the Arase satellite remained in the magnetosphere on its outbound orbit between 11.6 and 11.8 magnetic local time (MLT; in hours) at a magnetic latitude (MLAT) of approximately 25°. After 06:52:50 UT, electron fluxes in a broad energy range below 1 keV increased significantly and ion fluxes subsequently followed the electron variation, while the local magnetic field remained northward ($B_{Z,GSM} > 0$, where $B_{Z,GSM}$ is the Z-component of the local magnetic field in the geocentric solar magnetospheric (GSM) coordinate system) (Fig. 2a-d,f). The flux enhancement indicates that the Arase satellite entered the low-latitude boundary layer (LLBL), where the local magnetic field originates from the Earth's main magnetic field (a northward magnetic field), but one end of a magnetic field line is connected to the solar wind. In LLBL, Arase observed plasma originating from the magnetosheath, which is the region of solar wind decelerated and heated at the bow shock. After 07:04:37 UT (vertical line at the center of Fig. 2), multiple magnetopause crossings occurred at 12.0 MLT under solar wind dynamic pressure from 35 to 39 nPa and IMF-B_Z from − 27 to − 31 nT. The positive and negative excursions of $B_{Z,GSM}$ (orange line in Fig. 2f) indicate that the magnetopause oscillated back and forth around the position of Arase, so that the satellite was intermittently observing the LLBL and then the magnetosheath boundary layer (MSBL, a southward magnetic field originating from IMF). Since the magnetopause is the boundary of the Earth's main magnetic field and IMF, it is located between LLBL and MSBL. The first magnetopause crossing by the Arase satellite occurred at a radial distance of 4.96 R_E, which is the innermost spacecraft observation of the magnetopause ever available in the literature[18–20]. Energetic O^+ ions exhibited parallel flows in the LLBL and anti-parallel flows in the MSBL with sudden flux enhancements (Fig. 2e,f). The unidirectional enhanced fluxes represent ion reconnection jets because ions launched from a lower latitude become parallel flows in the northward background magnetic field and anti-parallel flows in the

southward background magnetic field in the northern hemisphere. Furthermore, in MSBL, one end of a magnetic field line is connected to the magnetosphere, and thus high-energy ($\gtrsim$ 60 keV) protons continue to be detected (Fig. 2c). After 07:13:05 UT (vertical line on the right side in Fig. 2), the Arase satellite finally entered the magnetosheath proper, and the magnetic field was continuously directed southward (Fig. 2f). Magnetic field lines were no longer connected to the magnetosphere in the magnetosheath, and hence Arase did not observe any enhanced fluxes of O^+ ions and the high-energy protons, both of which originate from the magnetosphere (Fig. 2c, e).

Figure 1 summarizes the magnetopause crossing by the Arase satellite on May 11, 2024. The magnetopause is represented by a dashed line at ~ 5 R_E in Fig. 1. LLBL and MSBL lie on the earthward side and sunward side of the magnetopause under a southward IMF. Within the LLBL and MSBL, the magnetic fields are directed northward and southward, respectively. In these regions, the magnetic field lines of the magnetosphere are connected to the magnetosheath, and the plasmas from both the magnetosphere and the magnetosheath are mixed. Thus, energetic O^+ ions and protons still exist in LLBL and MSBL. The magnetospheric electrons at > 10 keV exhibit a rapid decrease in their flux at the middle of LLBL (at 06:56 UT). This is consistent with the fact that the parallel velocity of the magnetospheric electrons is sufficiently high to escape into interplanetary space along an open magnetic field line. The Arase satellite observed these features of the boundary layers as it moved sunward (the right-hand side of Fig. 1).

Discussion and Conclusions

The *in situ* observation by the Arase satellite further provides insight into the mechanism of magnetospheric erosion during the May 2024 super geomagnetic storm. Figure 3a shows the radial distributions of the local magnetic pressure (P_B, blue line), O^+ thermal pressure (P_{O+}, green line), and total pressure ($P_B + P_{O+}$, red line) during the interval from 06:11 UT to 07:34 UT on May 11, 2024. In this interval, the O^+ thermal pressure was a good proxy for the ion thermal pressure on the magnetospheric side because ring current O^+ ions dominated the ion thermal pressure (80–90% of ion thermal pressure) in the magnetosphere (Supplementary Information Fig. 1. See Methods for details of the pressure calculation). The O^+ dominance enabled us to distinguish the magnetospheric ion thermal pressure from the solar wind ion (H^+) thermal pressure. In Fig. 3a, as the Arase satellite moved outward (sunward) in Earth's strong main magnetic field, the magnetic pressure and the total pressure decreased in the magnetosphere and LLBL. In the vicinity just inside the magnetopause, the total pressure becomes approximately equal to the solar wind dynamic pressure for the magnetopause crossing at 07:03 UT (dashed horizontal line). Therefore, we consider that the pressure balance between solar wind dynamic pressure and magnetospheric pressure was approximately satisfied during the magnetopause crossing by Arase.

As shown in Fig. 3a, the magnetic field is the primary factor of the pressure balance between the solar wind and the magnetosphere. To examine the details of the magnetic pressure variations, we subtracted

the magnetic field calculated by the IGRF-14 geomagnetic field model[21] from the measured local magnetic field (Fig. 3b). Because the IGRF-14 model describes Earth's main magnetic field, the difference between the local magnetic field and the IGRF-14 model field represents the external magnetic field generated by magnetospheric current systems and local magnetospheric dynamics, such as magnetic reconnection. At > 4.2 R_E, the decrease in the local magnetic field intensity became prominent, but its position was still far from the magnetopause. The magnitude of the decrease reached approximately 60 nT at 4.5 R_E. Fluctuations in the magnetic field intensity were then observed at larger radial distances. In the LLBL, sharp transient depletions were repeatedly detected. The white line in Fig. 3b represents a linear fit to the variation in the magnetic field intensity within the LLBL. The slope of the fitting line shows that the local magnetic field intensity, on average, decreased by ~ 41 nT within LLBL. There is an estimation error of ± 6.5 nT in the amplitude of the decrease, caused by the 1-sigma uncertainty of the inclination of the linear fitting. Fluctuations in the magnetic field intensity intensified in the MSBL, and finally, a strong compressed magnetic field with smaller fluctuations were observed in the magnetosheath.

The decrease in the magnetic field intensity deep inside the magnetosphere (Fig. 3b) clearly shows the dominant contribution of the magnetospheric currents to magnetic field variations. This is consistent with the fact that the magnetopause reconnection is a localized process around the magnetopause and cannot account for the radially-wide decrease in the magnetic field intensity. Moreover, the decrease in the magnetic field intensity beyond the center of the ring current at ~ 3 R_E (Supplementary Information Fig. 1) indicates that the Region-1 field-aligned current and/or the cross-tail current counteract the northward magnetic field (upward light blue arrows in Fig. 1) generated by the magnetopause current and dayside ring current. Therefore, our findings provide the first experimental evidence of the significant contribution of magnetospheric currents to magnetopause erosion around the low-latitude magnetopause during super geomagnetic storms. Given that the decrease in the magnetic field intensity deep inside the magnetosphere is attributed to the magnetospheric currents, the Region-1 field-aligned current and/or the cross-tail current caused a decrease of > 60 nT if we take the magnetopause current and the ring current into account.

In addition, the gradual decrease in the magnetic field intensity around the magnetopause also indicates another contributing factor associated with the magnetopause. The transient depletion of the magnetic field intensity in the LLBL was caused by an approach to MSBL, where the magnetic field was much weaker than LLBL. The transient magnetic field depletion and the multiple magnetopause crossings can be attributed to the transient removal of the magnetic flux caused by repeated magnetopause reconnections, as described in previous studies[3–7]. Therefore, we conclude that magnetopause reconnection also contributed to the magnetopause erosion. Given that the northward magnetic field generated by the magnetopause current did not vary largely within the thin LLBL, its average contribution to the decrease in the magnetic field intensity derived from linear fitting (~ 41 [± 6.5] nT) is secondary compared to those of the Region-1 field-aligned current and/or the cross-tail current ($\gtrsim$ 60 nT). The summation of the decrease in the magnetic field intensity discussed here is $\gtrsim$ 100 nT, and hence, $\gtrsim$60%

of the decrease in the magnetic field intensity can be attributed to the Region-1 field-aligned current and/or the cross-tail current on average.

The final remarkable feature of the magnetopause crossing is the ring current ions near the magnetopause. In previous studies, ring current ions were considered to play a role in the pressure balance at the magnetopause[22,23]; however, no studies have directly evaluated the contribution from the ring current thermal pressure during a super geomagnetic storm. In this study, the O^+ thermal pressure was significantly high (~ 7 nPa) even at the magnetopause (Fig. 3a), indicating that the magnetospheric ring current ions partially pushed back the solar wind exerted on the magnetopause. Approximately 20% of the solar wind dynamic pressure (~ 35 nPa) was directly balanced by the ring current ion thermal pressure. This result suggests that the heavy ion originating from the planetary atmosphere is one of the key factors controlling the magnetopause location during highly disturbed times.

The present study has suggested that magnetospheric currents are the primary cause of intense magnetopause erosion during the May 2024 super geomagnetic storm. The effect of the magnetospheric currents on the magnetopause erosion should be taken into account more seriously because it can increase the risk of solar energetic particle (SEP) exposure at mid-latitudes. The magnetopause is an approximate boundary of open and closed magnetic field lines (Fig. 1), and hence intense magnetopause erosion causes an equatorward shift of the penetration region of SEPs coming from the solar wind through an open field line. The solid line in the top panel of Fig. 4 shows the Altitude-Adjusted Corrected Geomagnetic (AACGM) latitude of the magnetic footprint of the magnetopause detected by Arase under a steady IMF-$B_{Z,GSM}$ and P_{SW} (see Method section for details of the determination of the equator boundary of SEPs) during this storm. The magnetic field line was calculated using the Tsyganenko and Sitnov (2005) model[24]. In the dayside topside ionosphere, the Polar Orbiting Environmental Satellite (POES) 18 detected SEPs (> 6.9 MeV protons) in the polar region (color-coded map in Fig. 4). The magnetopause footprint shows variations synchronized with the equatorward boundary of SEPs, reaching down to 60° AACGM latitudes during the storm main phase. Therefore, the significant equatorward expansion of the SEPs indicates that the magnetospheric currents can surely increase the risk of aircraft exposure to SEPs, which leads to glitches in flight-control data and radiation exposure for the crew at mid-latitudes during super geomagnetic storms.

Methods

Arase Satellite Data

The Arase satellite is equipped with several instruments for the measurement of charged particles. MEP-e[25] measures energetic electrons between 7.0 keV and 87.5 keV with 15 energy steps. LEP-e[26] measures lower energy electrons between 0.067 keV and 19.1 keV with 28 energy steps. MEP-e and LEP-e cover a solid angle of 4π sr using spacecraft spin motion and provide 8-sec (spin-averaged) omnidirectional electron flux data. We used MEP-i[27] and LEP-i[28] data for the analysis of ions. MEP-i

measures H^+, He^{++}, He^+, O^{++}, O^+, and $N_2^+/NO^+/O_2^+$ between 9.6 keV/q and 184.2 keV/q with 15 energy steps. LEP-i measures H^+, He^+, and O^+ between 0.0039 keV and 25.5 keV with 29 energy steps. Both instruments have two observational modes, normal mode and time-of-flight (TOF) mode. In the normal mode, 3D velocity distributions are provided with an angular resolution of 22.5° in the azimuthal and polar directions. While LEP-i was operating in the normal mode during the period considered in this study, MEP-i was in the TOF mode, in which 3D velocity distributions of ions are not provided. Because MEP-i in the TOF mode provides energy spectra of omnidirectional ion fluxes as well as TOF data, we used the omnidirectional ion flux data to calculate ion thermal pressure by combining the MEP-i and LEP-i data obtained in the two different modes. In the calculation of ion thermal pressure, we used MEP-i 32-s TOF-mode omnidirectional fluxes between 22.1-184.2 keV/q and LEP-i 8-s normal-mode omnidirectional fluxes between 0.035 keV and 19.2 keV with an assumption of an isotropic pitch angle distribution:

$$P_{s,\mathrm{LEP-i}} \simeq \frac{4\pi}{3}\sqrt{2m_s}\sum_{0.035\ \mathrm{keV}}^{19.2\ \mathrm{keV}}\sqrt{E}J_{s,\mathrm{LEP-i}}(E)\,\Delta E,$$

$$P_{s,\mathrm{MEP-i}} \simeq \frac{4\pi}{3}\sqrt{2m_s}\sum_{22.1\ \mathrm{keV/q}}^{184.2\ \mathrm{keV/q}}\sqrt{E}J_{s,\mathrm{MEP-i}}(E)\,\Delta E,$$

$$P_s = P_{s,\mathrm{LEP-i}} + P_{s,\mathrm{MEP-i}},$$

where m_s is the mass of ion species s, E is the ion energy, and ΔE is the energy step width. To apply the trapezoidal rule to the pressure calculation, E and ΔE were obtained from $\log_{10}E = (\log_{10}E_i + \log_{10}E_{i+1})/2$, $\Delta E = E_{i+1} - E_i$, where i represents the i-th energy step. $J_{s,\mathrm{LEP-i/MEP-i}}$ is the omnidirectional differential number flux of LEP-i/MEP-i obtained from $J_{s,\mathrm{LEP-i/MEP-i}}(E) = (J_{s,\mathrm{LEP-i/MEP-i}}(E_i) + J_{s,\mathrm{LEP-i/MEP-i}}(E_{i+1}))/2$. P_s is the ion thermal pressure obtained by combining the LEP-i pressure ($P_{s,\mathrm{LEP-i}}$) and MEP-i pressure ($P_{s,\mathrm{MEP-i}}$) of ion species s.

Magnetopause Location under a Steady Solar Wind

To exclude dynamic variations of the magnetopause location in the comparison analysis between the Arase and POES observations, we used the magnetopause location under a steady solar wind. The criteria for a steady solar wind are as follows. For the solar wind data during the past 10 min, (i) IMF-$B_{Z,GSM}$ and P_{SW} variation is less than 50% of an average over the past 10 min, (ii) more than 5 data points (> 5 min) of IMF-B_Z and P_{SW} pressure have finite values, (iii) the northward-southward direction of IMF does not change. In Supplementary Information Fig. 2, the steady solar wind selected with these criteria is represented in blue-filled circles. The magenta-filled circles represent the period of an unsteady solar wind. During the steady solar wind, Arase crossed the magnetopause six times, as shown in Supplementary Information Fig. 2. Because IMF-B_Z was southward during these periods, we considered that the magnetopause corresponds to a step-like variation between the northward/southward magnetic field at Arase.

POES-18 Satellite Data and Equator Boundary of SEPs

The POES-18 satellite is a Low Earth Orbit (LEO) satellite at polar orbits with an orbital period of ~ 100 min. It is equipped with the MEPED instrument of the Solar Environment Monitor (SEM-2) instrument package, which measures trapped and precipitating fluxes of protons from 30 keV to > 6,900 keV[29]. The equatorward boundary of SEPs was determined from the lowest latitude of the latitudinal bins with proton fluxes of > 0.1 $s^{-1}cm^{-2}sr^{-1}keV^{-1}$ on each spacecraft orbit at AACGM latitudes of > 55° in the northern hemisphere.

Declarations

Data Availability

The ERG Science Center[30], which is operated by ISAS/JAXA and Nagoya University, archives the science data of the Arase satellite. The data used in the present study are publicly available from the ERG Science Center website (https://ergsc.isee.nagoya-u.ac.jp/index.shtml.en). This study used the MGF Level-2 8 sec spin-averaged v04.06 data[31,32], MEP-i Level-2 omnidirectional flux v02_02 data[27,33], MEP-e Level-2 omnidirectional flux v01_02 data[28,37], LEP-i Level-2 omnidirectional flux v03_00 data[28,35], LEP-e Level-2 omnidirectional flux v04_01 data[26,36], Level-2 definitive orbital v05 data[37], and Level-3 TS04 model v01 data[38]. The OMNI 1-min solar wind v01 data set[39] was obtained from the Goddard Space Flight Center Space Physics Data Facility OMNIWeb (http://omniweb.gsfc.nasa.gov). The Dst index[13] was provided by the World Data Center for Geomagnetism, Kyoto (http://wdc.kugi.kyoto-u.ac.jp/wdc/Sec3.html). The POES-18 SEM-2 MEPED 2-s flux data (v01), which are originally provided by National Oceanic and Atmospheric Administration (NOAA), are available at Coordinated Data Analysis Web (CDAWeb) https://cdaweb.gsfc.nasa.gov/istp_public/data/noaa/noaa18/sem2_fluxes-2sec/.

Code Availability

The Space Physics Environment Data Analysis System (SPEDAS)[40] software (version 6.1) was used in the analysis. The software is publicly available at https://themis.ssl.berkeley.edu/socware/.

Acknowledgements

We thank T. Segawa (Technical Center, Nagoya University) for maintaining the data archiving system at the ERG Science Center. We thank Editage for English language editing.

Funding Declaration

The LEPe development is supported by the Academia Sinica, National Cheng Kung University, and the Ministry of Science and Technology of Taiwan under Contract No. MOST 105-3111-Y-001-042 and MOST 106-2111-M-001-011. A.S. was supported by JSPS KAKENHI Grant Numbers 24K07112, 24K00898, and 23K22555.

Contributions

K.Y., Y.M., and N.K. conceived this study. K.Y. collected, analyzed data, and prepared the manuscript. K.Y., Y.M., N.K., A.S., and R.N. interpreted the result. A.M., M.T., K.Y. (MGF), S.Y., S.K., K.K., T.H. (MEP-e and MEP-i), K.A., Y.M. (LEP-i), Y.K., S.Y.W., S.W.Y.T., T.F.C., B.J.W., and C.W.J. (LEP-e) contributed to the instrument development, operation, data processing, and data quality assurance. I.S. and Y.M. led the ERG mission. All authors reviewed and improved the manuscript.

Additional Information

The authors declare no competing interests.

References

1. Chapman, S. & Ferraro, V. C. A. A new theory of magnetic storms. *Terr. Magn. Atmos. Electr.* **38**, 79–96 (1933).
2. Fairfield, D. H. Average and unusual locations of the Earth's magnetopause and bow shock. *J. Geophys. Res.* **76**, 6700–6716 (1971).
3. Aubry, M. P., Russell, C. T. & Kivelson, M. G. Inward motion of the magnetopause before a substorm. *J. Geophys. Res.* **75**, 7018–7031 (1970).
4. Russell, C. T. & Elphic, R. C. ISEE observations of flux transfer events at the dayside magnetopause. Geophys. Res. Lett. 6, 33–36 (1979).
5. Shue, J.-H. et al. A new functional form to study the solar wind control of the magnetopause size and shape. J. Geophys. Res. 102, 9497–9511 (1997).
6. Shue, J.-H. et al. Magnetopause location under extreme solar wind conditions. J. Geophys. Res. 103, 17691–17700 (1998).
7. Kim, H. et al. Relation between magnetopause position and reconnection rate under quasi-steady solar wind dynamic pressure. Earth Planets Space 76, 165 (2024).
8. Ober, D. M., Maynard, N. C., Burke, W. J., Wilson, G. R. & Siebert, K. D. “Shoulders” on the high-latitude magnetopause: Polar/GOES observations. *J. Geophys. Res.* **111**, A10213 (2006).
9. Samsonov, A. A., Bogdanova, Y. V., Branduardi-Raymont, G., Sibeck, D. G. & Toth, G. Is the relation between the solar wind dynamic pressure and the magnetopause standoff distance so straightforward? *Geophys. Res. Lett.* **47**, GL086474, e2019 (2020).
10. Wiltberger, M., Lopez, R. E. & Lyon, J. G. Magnetopause erosion: A global view from MHD simulation. J. Geophys. Res. 108, 1235 (2003).
11. Maltsev, Y. P. & Lyatsky, W. B. Field aligned current and erosion of the dayside magnetosphere[A1.1]. Planet. Space Sci. 23, 1257–1260 (1975).
12. Maltsev, Y. P., Arykov, A. A., Belova, E. G., Gvozdevsky, B. B. & Safargaleev, V. V. Magnetic flux redistribution in the storm time magnetosphere. J. Geophys. Res. 101, 7697–7704 (1996).

13. World Data Center for Geomagnetism, Kyoto, M. Nose, T. Iyemori, M. Sugiura, T. Kamei, A. Matsuoka, S. Imajo, and T. Kotani (2015), Geomagnetic AE index, doi:10.17593/15031-54800 [Data set].
14. Echer, E., Gonzalez, W. D. & Tsurutani, B. T. Interplanetary conditions leading to superintense geomagnetic storms (DST ≤ − 250 nT) during solar cycle 23. *Geophys. Res. Lett.* **35**, 6 supplement 03 (2008).
15. Miyoshi, Y. et al. Geospace exploration project ERG. Earth Planets Space 70, 101 (2018a).
16. Hayakawa, H. et al. The solar and geomagnetic storms in 2024 may: A flash data report. *Astrophys. J.* **979**, 49 (2025).
17. Kwak, Y. S. et al. Observational overview of the May 2024 G5-level geomagnetic storm: From solar eruptions to terrestrial consequences. *J. Astron. Space Sci.* **41**, 171–194 (2024).
18. Hoffman, R. A. et al. Explorer 45 (S^3-A) observations of the magnetosphere and magnetopause during the August 4–6, 1972, magnetic storm period. *J. Geophys. Res.* **80**, 4287–4296 (1975).
19. Chang, S.-W. et al. Energetic magnetosheath ions connected to the Earth's bow shock: Possible source of cusp energetic ions. *J. Geophys. Res.* **105**, 5471–5488 (2000).
20. Goldstein, J. et al. Cross-scale observations of the 2015st. Patrick's day storm. *JGR Space Physics* **122**, 368–392 (2017).
21. International Association of Geomagnetism and Aeronomy. IGRF-14. *Zenodo*, (2024).
22. Dmitriev, A., Suvorova, A. & Chao, J.-K. A predictive model of geosynchronous magnetopause crossings. *J. Geophys. Res.* **116**, A05208 (2011).
23. Machková, A., Němec, F., Němeček, Z. & Šafránková, J. On the influence of the Earth's magnetic dipole eccentricity and magnetospheric ring current on the magnetopause location. *JGR Space Physics* **124**, 905–914 (2019).
24. Tsyganenko, N. A. & Sitnov, M. I. Modeling the dynamics of the inner magnetosphere during strong geomagnetic storms. *J. Geophys. Res.* **110**, A03208 (2005).
25. Kasahara, S. et al. Medium-energy particle experiments—Electron analyzer (MEP-e) for the exploration of energization and radiation in geospace (ERG) mission. *Earth Planets Space* **70**, 69 (2018a).
26. Kazama, Y. et al. Low-energy particle experiments–electron analyzer (LEPe) onboard the Arase spacecraft. *Earth Planets Space* **69**, 165 (2017).
27. Yokota, S. et al. Medium-energy particle experiments–ion mass analyzer (MEP-i) onboard ERG (Arase). *Earth Planets Space* **69**, 172 (2017).
28. Asamura, K., Kazama, Y., Yokota, S., Kasahara, S. & Miyoshi, Y. Low-energy particle experiments–ion mass analyzer (LEPi) onboard the ERG (Arase) satellite. *Earth Planets Space* **70** (2018a).
29. Evans, D. S. & Greer, M. S. *Polar orbiting environmental satellite space environment Monitor-2 instrument descriptions and archive data documentation 1.4*, Space Environ. Lab., Boulder, Colorado (*NOAA Tech*, 2004).
30. Miyoshi, Y. et al. The ERG Science Center. *Earth Planets Space* **70**, 96 (2018b).

31. Matsuoka, A. et al. The ARASE (ERG) magnetic field investigation. *Earth Planets Space* **70**, 43 (2018).
32. Matsuoka, A. et al. The MGF instrument Level-2 spin-averaged magnetic field data of Exploration of energization and Radiation in Geospace (ERG) Arase satellite, (2018). [Data set]. Accessed on 2026-January 20.
33. Yokota, S. et al. The MEP-i instrument Level-2 omni-directional flux data of Exploration of energization and Radiation in Geospace (ERG) Arase satellite, (2018). [Data set]. Accessed on2026-January 20.
34. Kasahara, S. et al. The MEP-e instrument Level-2 omni-directional flux data of Exploration of energization and Radiation in Geospace (ERG) Arase satellite, (2018b). [Data set]. Accessed on2026-January 20.
35. Asamura, K., Miyoshi, Y. & Shinohara, I. The LEPi instrument Level-2 omniflux data of Exploration of energization and Radiation in Geospace (ERG) Arase satellite, (2018b). [Data set]. Accessed on2026-January 20.
36. Wang, S.-Y. et al. The LEPe instrument level-2 omni-directional flux data of Exploration of energization and Radiation in Geospace (ERG) Arase satellite, (2018). [Data set]. Accessed on2026-January 20.
37. Miyoshi, Y., Shinohara, I. & Jun, C.-W. The Level-2 orbit data of Exploration of energization and Radiation in Geospace (ERG) Arase satellite, (2018c). [Data set]. Accessed on2026-January 20.
38. Miyoshi, Y., Shinohara, I. & Jun, C.-W. The Level-3 orbit data of Exploration of energization and Radiation in Geospace (ERG) Arase satellite, (2018d). [Data set]. Accessed on2026-January 20.
39. Papitashvili, N. E. & King, J. H. OMNI 1-min Data Set. [Data set] (NASA Space Physics Data Facility, 2020). Accessed on2026-January 20.
40. Angelopoulos, V. et al. The Space Physics Environment Data Analysis System (SPEDAS). *Space Sci. Rev.* **215**, 9 (2019).
41. Lin, R. L., Zhang, X. X., Liu, S. Q., Wang, Y. L. & Gong, J. C. A three-dimensional asymmetric magnetopause model. *J. Geophys. Res.* **115**, A04207 (2010).

Figures

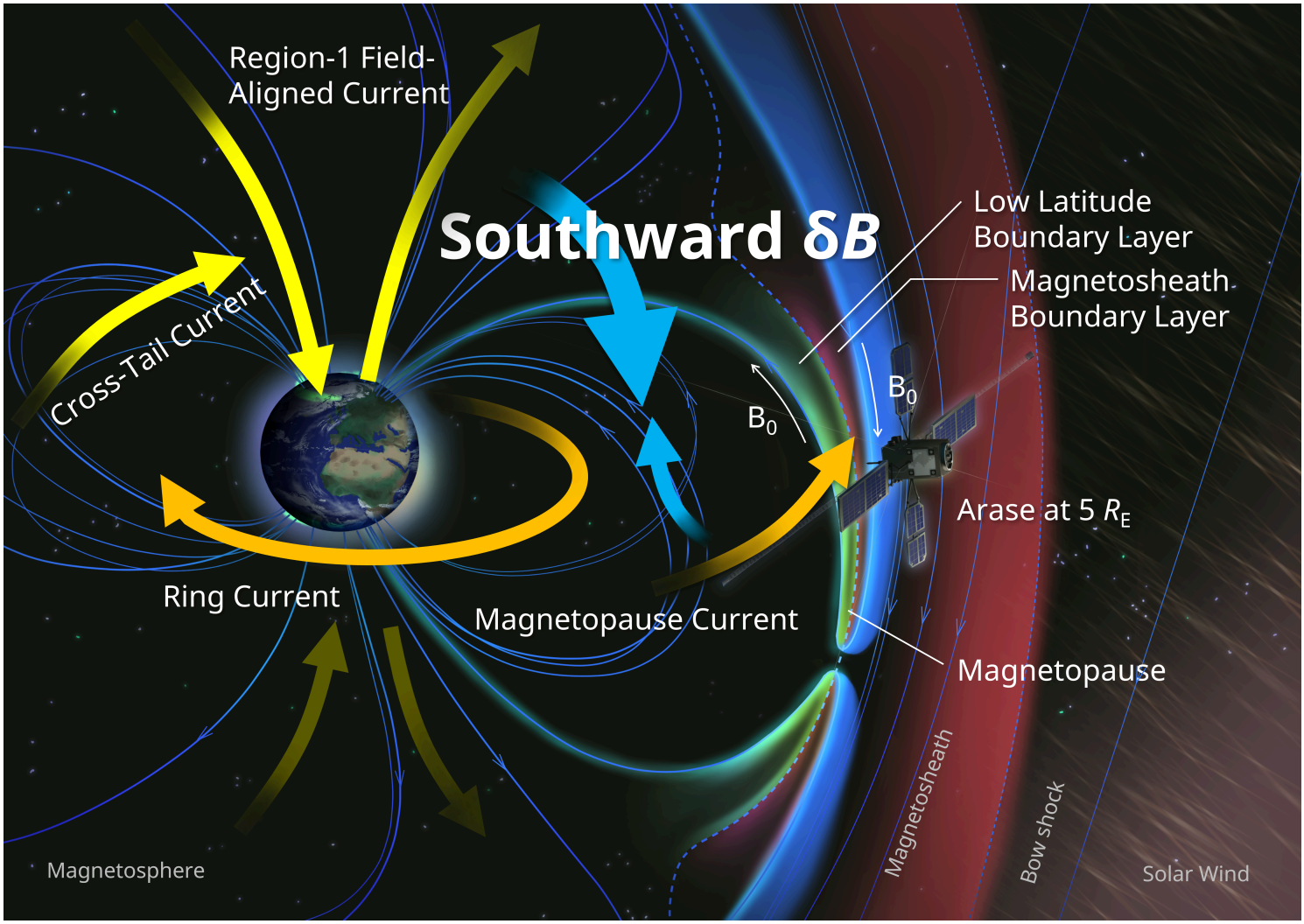


Figure 1

Schematic view of the Arase satellite observation of the magnetopause during the May 2024 super geomagnetic storm. Light blue arrows represent the magnetic field perturbation generated by magnetospheric currents, which are indicated by yellow arrows.

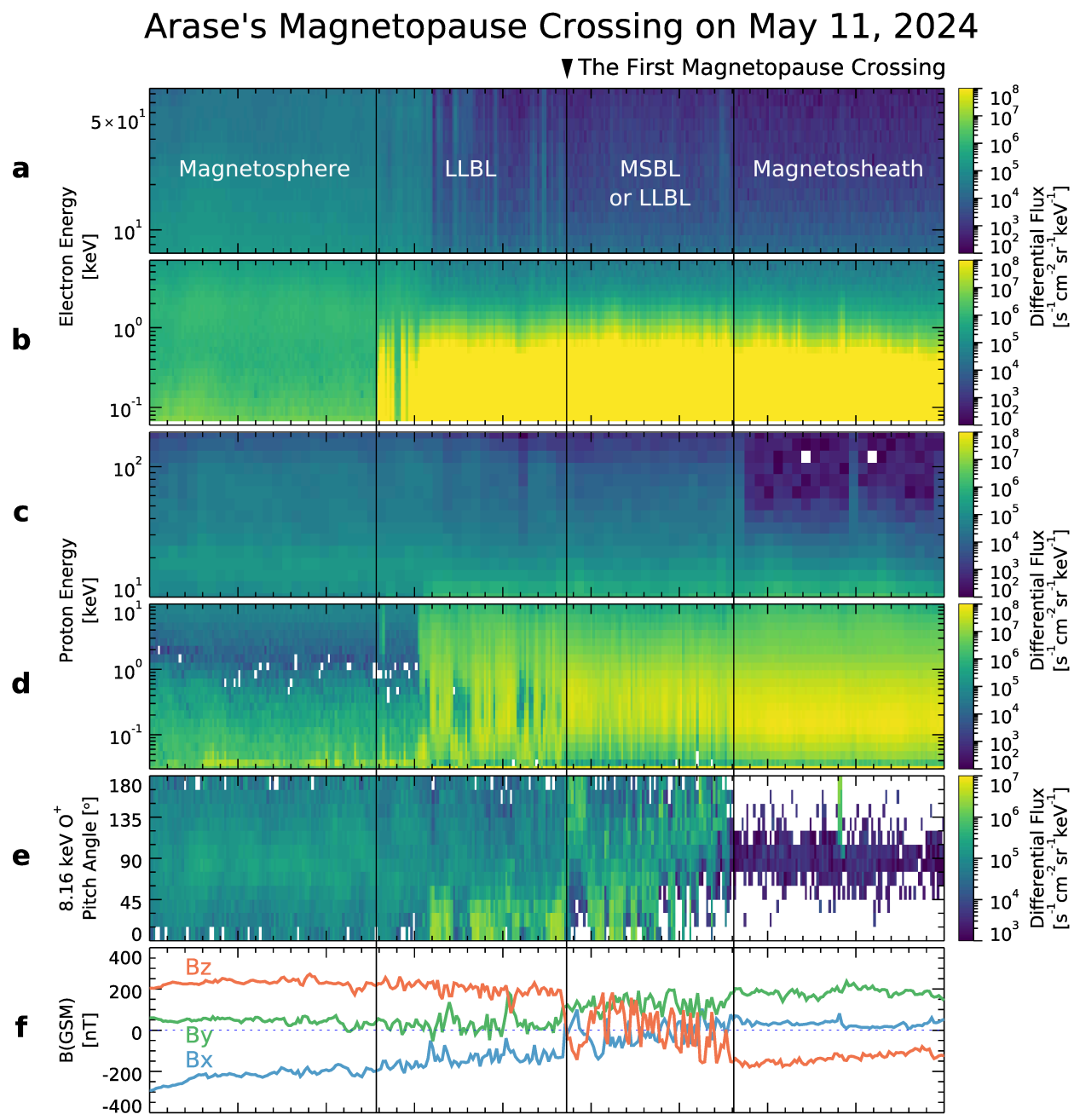


Figure 2

***In situ* observation of the intensely eroded magnetopause by the Arase satellite at 5 R_E during a super geomagnetic storm on May 11, 2024. a, b,** Energy-time spectrograms of electron omnidirectional differential fluxes measured by MEP-e[25] and LEP-e[26]. **c, d,** Energy-time spectrograms of proton omnidirectional differential fluxes measured by MEP-i[27] and LEP-i[28]. **e,** Pitch angle distributions of

differential fluxes of 8.16 keV O^+ ion measured by LEP-i. **f,** Magnetic field vectors measured by MGF[31] in the GSM coordinates.

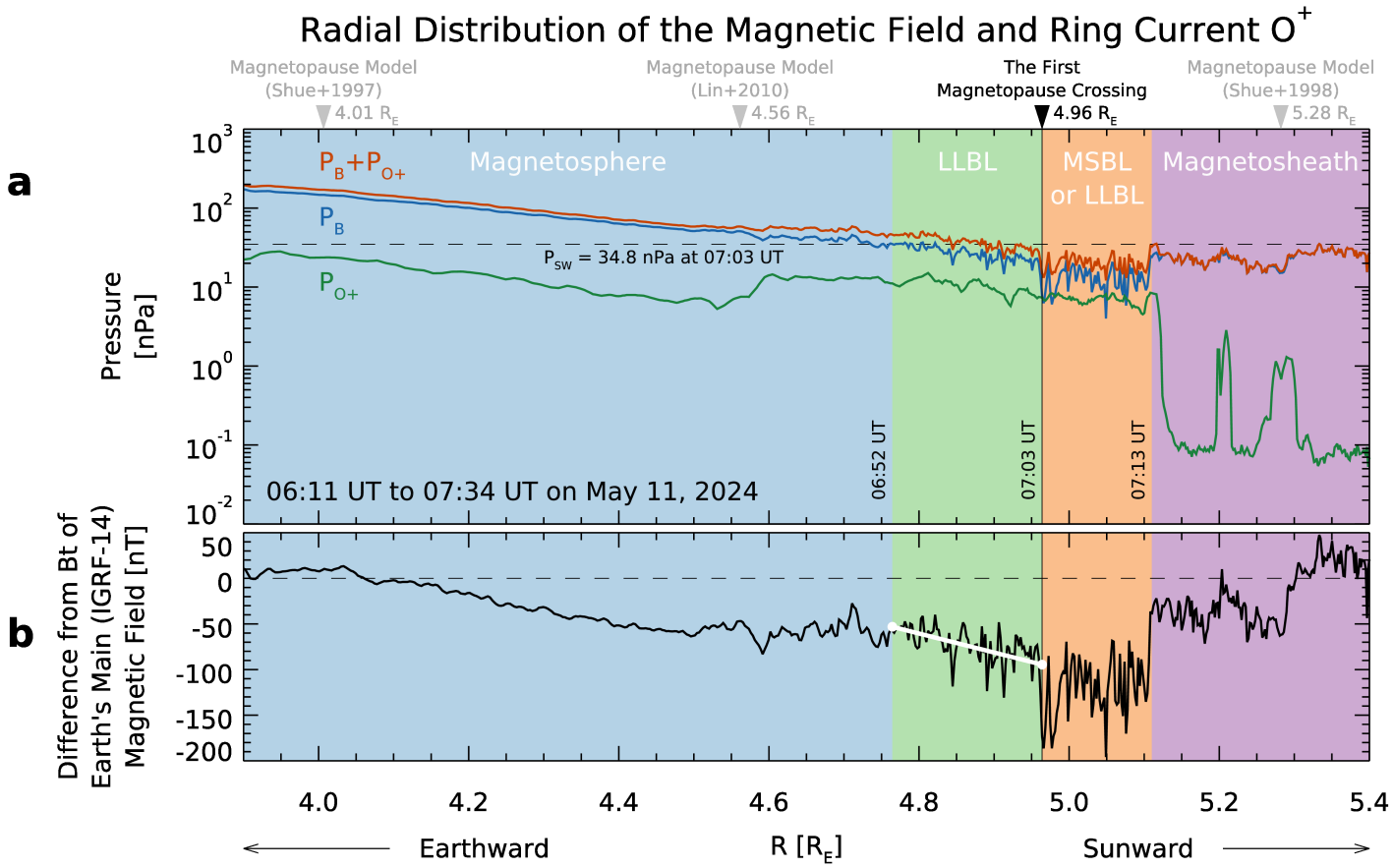


Figure 3

Radial distribution of magnetic field intensity, showing large decreases in the magnetosphere and the boundary layers. a, Magnetic field pressure (blue line), O^+ ion thermal pressure (green line), and the sum of them (red line) calculated from LEP-i (0.035–19.2 keV) and MEP-i (22.1–184.2 keV) measurements. Magnetopause locations predicted by empirical models[5,6,41] are shown at the top for reference. **b,** Differences between the observed magnetic field intensity and the IGRF-14 model. The white line in panel b represents the linear fit in the low-latitude boundary layer, showing the baseline of the magnetic field variations.

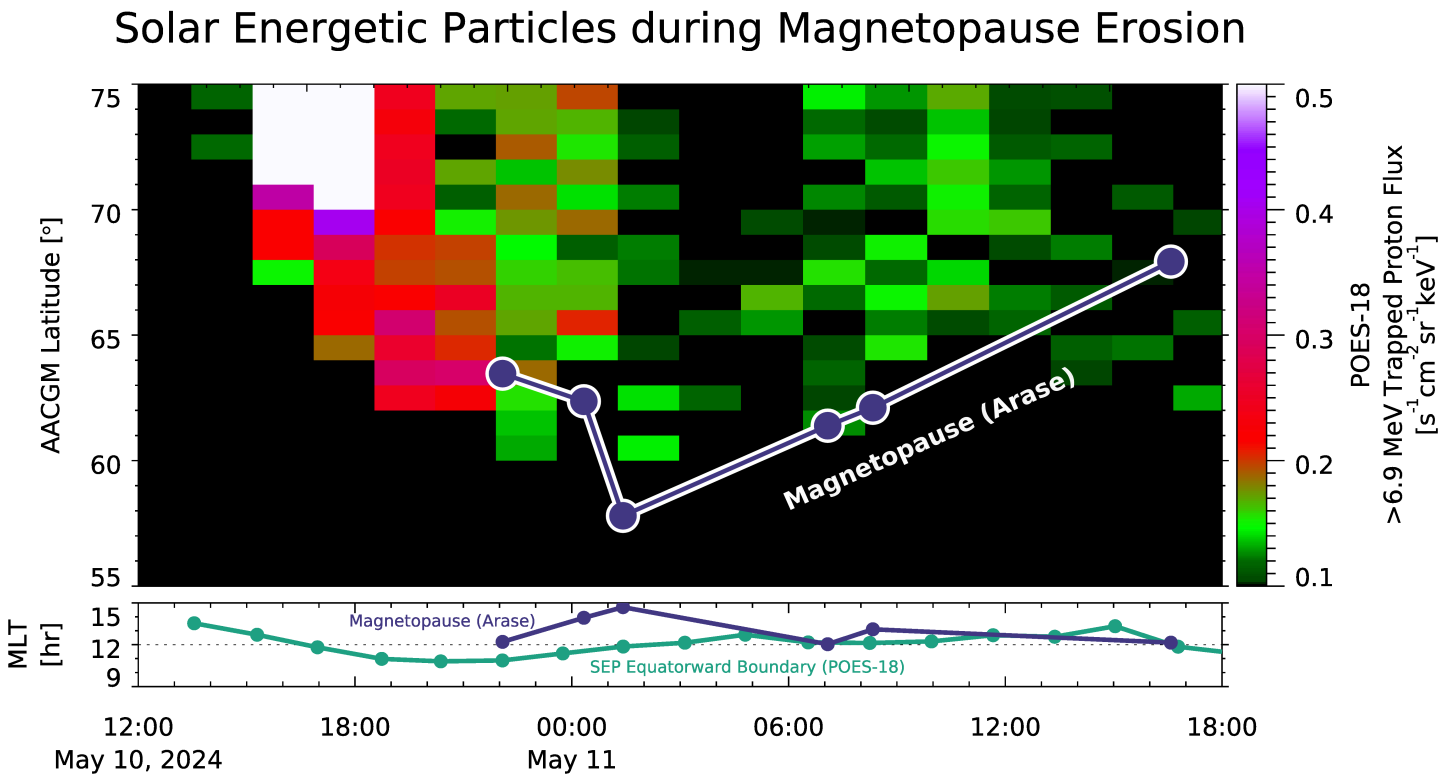


Figure 4

The latitudinal distribution of SEP proton fluxes of > 6.9 MeV (color-coded map) measured by Medium Energy Proton and Electron Detector (MEPED) [29] onboard POES-18. The ionospheric footprint of the magnetopause detected by Arase under a relatively steady solar wind (purple solid circles) is also shown. The MLTs of the magnetopause and the equatorward boundary of SEPs are presented in the lower panel.

Supplementary Files

This is a list of supplementary files associated with this preprint. Click to download.

- 2026SciRepMPCSupplementaryInformationv2.0.0.docx